Research Square

Preprints are preliminary reports that have not undergone peer review.
They should not be considered conclusive, used to inform clinical practice,
or referenced by the media as validated information.

Metal Complexes of Tridentate Schiff Base: Synthesis, Characterization, Biological Activity and Molecular Docking Studies with COVID-19 Protein Receptor

mohamed m Omar
Cairo University Faculty of Science
Walaa H. Mahmoud
Cairo University Faculty of Science
Yasmin mamdoh hussien Ahmed (yassmine@sci.cu.edu.eg)
Cairo University Faculty of Science https://orcid.org/0000-0001-6951-7735
Gehad G. Mohamed
Cairo University Faculty of Science

Original Research Full Papers

Keywords: Metal complexes, Schiff base ligand, spectroscopic analysis, Microbial and anticancer activity, molecular docking of COVID-19, density functional theory.

Posted Date: February 18th, 2021

DOI: https://doi.org/10.21203/rs.3.rs-207632/v1

License: This work is licensed under a Creative Commons Attribution 4.0 International License.
Read Full License

Metal complexes of Tridentate Schiff base: Synthesis, Characterization, Biological Activity and Molecular Docking Studies with COVID-19 Protein Receptor

M.M. Omar[1], Walaa H. Mahmoud[1], Yasmin M. Ahmed[1]*, Gehad G. Mohamed[1]

[1] Chemistry Department, Faculty of Science, Cairo University, Giza, 12613, Egypt.

Corresponding author e.mail: yassmine@sci.cu.edu.eg

Abstract

Mononuclear chelates of Cr(III), Mn(II), Fe(III), Ni(II), Cu(II), Zn(II) and Cd(II) resulting from new tridentate Schiff base ligand , 4-((1-(5-acetyl-2,4-dihydroxyphenyl)ethylidene)amino)-1,5-dimethyl-2-phenyl-1H-pyrazol-3(2H)-one, were synthesized and characterized via various spectroscopic methods. Metal to ligand ratio was found to be 1:1, which was revealed via elemental analysis. IR has sharp out that the coordination of the ligand towards the metal ions was carried out via NOO atoms. UV-Vis, ^{1}HNMR spectral data, molar conductance measurements, BET surface area, melting points and theoretically through density function theory were used such as characterizing techniques in supporting of further interpretation of the complexes structures. The complexes were octahedral except Cu(II) and Ni(II) complexes were tetrahedral as suggested through the magnetic moment measurement. The complexes were found to have surface area, pore volume and particle radius 23-176 m^2 g^{-1}, 0.02-0.33 cc/g and 8.71-4.32 nm, respectively, as pointed out from BET measurement. Schiff base ligand and its metal complexes were tested in vitro to estimate their bactericidal activity opposed to Gram-negative and Gram-positive bacteria and antifungal organisms. In the recent incident of a novel coronavirus (SARS-CoV-2) spreads, antiviral drug detection is of most importance. MOE 2008 was used headed for screen potential drugs with molecular docking by the structural protein and non-structural protein sites of new coronavirus and the study was constructed to molecular docking without validation through MD simulations. Interactions with the main protease may play a key role in fighting against viruses**.**

KEYWORDS

Metal complexes, Schiff base ligand, spectroscopic analysis, Microbial and anticancer activity, molecular docking of COVID-19, density functional theory.

1. Introduction

Schiff base is identified in the name of Hugo Schiff, who initially reported the reversible acid-catalyzed condensation reaction involving primary amine plus carbonyl compounds [1]**.**

The chemistry of metal complexes as a result of Schiff base ligands containing nitrogen and oxygen such as donor atoms has sustained to attract the interest of researchers. Ligands are recognized to coordinate to metal atom in various ways underneath different reaction conditions. ligands are derived as of the condensation reaction of primary amines and aldehydes.

One of the most important areas of research on the Schiff base metal complexes is their biological activity with the major purpose being the discovery of harmless and helpful therapeutic agents used for the treatment of bacterial infections and cancers. Numbers of Schiff base metal complexes have varied spectrum of pharmaceutical activities. For example, transition metal complexes of Schiff base ligands bearing "N" and "O" donor atoms are extremely focal as a result of their biological properties, for instance antibacterial, anticonvulsant, antifungal, anti-inflammatory, antioxidant, antitubercular, analgesic and anthelmintic [2].

Lately, the new coronavirus (2019-nCoV) appeared inside Hubei province, P.R. China. The whole-genome chain of 2019-nCoV was initially released on January 10, 2020. 2019-nCoV has a broad range of infection of mammals, plus humans. This characteristic of transmission leads to the probability of transmission from animals to people. The 2019-nCoV, identified as strict acute respiratory syndrome coronavirus (SARS-CoV-2) is vastly transmittable and could lead to mild to severe respiratory tract infections. The reach of 2019-nCoV has drawn numerous attentions. After that anxieties worldwide, since 2003 humans has faced two coronavirus-related crises. Difficult acute respiratory syndrome coronavirus (SARS-CoV) ruined out in 2003 and the Middle East Respiratory Syndrome Coronavirus (MERS-CoV) materialized in the Arabian Peninsula in 2012 by a fatality rate of 35% [3].

This work guided on the way to synthesis novel Schiff base ligand and its metal complexes. Several characterization analyses were used for identification of the structures of the prepared compounds. *In vitro* antimicrobial and anti-breast cancer activities had also been screened. The possible binding of the prepared compounds with crystal structure of the SARS-CoV-2 (COVID-19) major protease in complex with inhibitor UAW247 (PDB ID: 6XBH) was demonstrated.

2. Experimental

Totally chemicals consumed were of the analytical reagent grade (AR) and 4-amino antipyrine (Sigma) of the highest purity obtainable. The chemicals consumed entered which was provided from Strems Chemical Inc., 4,6-diacetylresorcinol (Sigma), $CrCl_3.6H_2O$, $MnCl_2.4H_2O$ and $FeCl_3$ (Sigma-Aldrich), $NiCl_2.6H_2O$, $CuCl_2.2H_2O$ and $ZnCl_2$ (BDH) and $CdCl_2$ (Merck).

Solvents of organically consumed were ethyl alcohol (95%) and N, N-dimethylformamide (DMF). Deionized water was usually consumed in every preparation [4, 6].

2.1 Solutions

Stock solutions of the Schiff base ligand (H_2L) and its metal complexes of 1×10^{-3} M were prepared via dissolving an accurately weighed amount in DMF. The molar conductivity, in that case was measured for the metal complex solutions. Dilute solutions of the Schiff base ligand and its metal complexes (1×10^{-4} M) were prepared by exact dilution from the before and prepared stock solutions for measuring their UV–Vis spectra. The absorption spectra were documented for 1×10^{-5} M. Solutions of the Schiff base ligand and its metal complexes in DMF and the spectra were scanned in the wavelength varies from 200 to 700 nm [4, 6].

2.2 Solution of anticancer study

A new stock solution (1×10^{-3} M) of Schiff base ligand in addition to its metal complexes (0.12×10^{-2} g L^{-1}) were prepared in the appropriate volume of DMF (90%). DMSO was used in cryopreservation of cells. RPMI-1640 medium was consumed. The medium was designed for culturing and maintain of the human tumor cell line. The medium was contributed in a powder shape. It was receiving ready along these lines:

10.4 g of medium was weighed, mixed with 2 g of sodium bicarbonate, done to 1 L per distilled water and shaken prudently until full dissolution. The medium was then pure through filtration in a Millipore bacterial filter (0.22 ml). The prepared medium was reserved in a refrigerator (4 ℃) and tested at methodical intervals for contamination. Beforehand use, the medium was warmed at 37 ℃ in a water bath and supplemented per penicillin–streptomycin and FBS. Sodium bicarbonate was consumed to the preparation of RPMI-1640 medium. Isotonic trypan blue solution (0.05%) was prepared within normal saline and were intended for possibility counting. FBS (10%, warm inactivated at 56 ℃ for 30 min), 100 units/mL penicillin and 2 mg/ml streptomycin were designed for the supplementation RPMI-1640 medium prior to utilize. Trypsin (0.25×10^{-1}% w/v) was used for the selection of cells. Acetic acid (1% v/v) was used for dissolving unbound SRB dye. SRB (0.40%) dissolved in 1% acetic acid was used evenly a protein dye. A stock solution of trichloroacetic acid (50%) was prepared then stored. A quantity of 50 µL of the stock was added to 200 µL of RPMI-1640 mediums apiece well to yield a final concentration of 10% used for protein precipitation. Isopropanol (100%) and ethanol (70%) were used. Tris base (10 mM; pH =10.50) was used for SRB dye solubilization. Tris base (121.10 g) was dissolved in 1000 ml of distilled waters and the pH was adjusted using hydrochloric acid (2 M) [4, 6].

2.3 Instrumentation

Micro analyses of nitrogen, hydrogen and carbon were approved by the Micro analytical Center, Cairo University, Egypt, via a CHNS-932 (LECO) Vario elemental analyzer. Analyses of the metals were performed through dissolving the solid complexes in concentrated HNO_3 and dissolving the remnants in deionized water. The metal content was carried out by inductively joined plasma atomic absorption spectrometry (ICP-AES), Egyptian Petroleum Research Institute. Fourier transform infrared (FT-IR) spectra were recorded with a Perkin-Elmer 1650 spectrometer (400–4000 cm^{-1}) in KBr pellets. ^1H NMR spectra, like solutions in DMSO-d_6, were chronicled per a300 MHz Varian-Oxford Mercury at room temperature consuming tetra-methyl silane such as an interior standard. Mass spectra were chronicled via the electron ionization technique at 70 eV through an MS-5988 GS-MS Hewlett-Packard instrument in the Microanalytical Center, National Center in place of Research, Egypt. UV–visible spectra were acquired including a Shimadzu UVmini-1240 spectrophotometer. Molar conductivities of 10^{-3} M solutions of the solid complexes in DMF were measured by a Jenway 4010 conductivity meter. Differential thermogravimetric (DTG) and thermogravimetric (TG) analyses of the solid complexes were carried out from room temperature to 1000 ºC by a Shimadzu TG-50H thermal analyzer. Antimicrobial measurements were carried out at the Microanalytical Center, Cairo University, Egypt. Anticancer activity experiments were performed by the National Cancer Institute, Cancer Biology Department, Pharmacology Department, Cairo University. The optical density (OD) of each in good form was measured spectrophotometrically at 564 nm with an ELIZA microplate reader (Meter tech. R960, Lewiston, USA). The surface area of compounds, gas adsorption measurements, was conducted via N_2 as the adsorptive gas at 77 K. The analysis was carried out via a Nova Touch LX2 analyzer and calculated based on the Brunauer-Emmett-Teller (BET) theory.

2.4 Synthesis of Schiff base ligand

The novel Schiff base ligand (H_2L) was synthesized through condensation of 4,6-diacetyl-resorcinol (4,6-DAR) in addition to 4-amino antipyrine. A solution of 4-amino antipyrine (15.45 mmol, 3.14 g) dissolved in ethanol was added drop wise to 4,6-DAR (15.45 mmol, 3 g) dissolved in DMF. The resulting mixture was stirred in reflux for about 4–5 hr at 100–150 ºC, through which orange solid compound was separated. It was filtered, washed, recrystallized beginning diethyl ether and dried in vacuum (Scheme 1).

2.5 Synthesis of metal complexes

Complexes of H_2L ligand were synthesized via the reaction of 1:1 molar mixture of warm ethanolic solution (60 ºC) of the suitable metal chloride (0.76 mmol) and H_2L (0.3 g, 0.76 mmol). The resulting mixture was stirred in reflux for 1 h where upon the complexes precipitated. They were collected via filtration and purified through washing several times by diethyl ether.

2.6 Pharmacology

2.6.1 Antibacterial activities

Antimicrobial activity of the probationary samples was established dusing a modified Kirby-Bauer disc diffusion technique [5]. Briefly, 100 µl of the test bacteria were grown in 10 ml of fresh media awaiting they reached a tally of approximately 108 cells/ml pro bacteria.100 µl of microbial suspension was diffused onto agar plates corresponding to the broth in which they were maintained. Isolated colonies of every one organism that may be playing a pathogenic part must be chosen from initial agar plates and tested for susceptibility through disc diffusion method. Plates inoculated Gram(−ve) bacteria for example *Escherichia coli* and Gram(+ve) bacteria for example *Staphylococcus aureus.* They were incubated at 35–37 ºC for 24–48 h and yeast for example *Candida albicans* incubated at 30 ºC for 24-48 hours and, then the diameters of the inhibition zones were measured in millimeters then the diameters of the inhibition zones were calculated in millimeters. Standard discs of amikacin (an antibacterial agent), served such as positive controls for antimicrobial activity, other than filter discs impregnated by 10 µl of solvent (distilled water, chloroform, DMSO) were used as a negative control. Blank paper disks (Schleicher & Schuell, SatisLda, Spain) in addition to a diameter of 8.0 mm were impregnated including 10 µ of testing concentration of the stock solutions (20 mg/ml). After a filter paper disc impregnated plus a tested chemical is placed on agar, the chemical will diffuse from the disc into the agar. This diffusion will place the chemical in the agar only around the disc. The solubility of the chemical and its molecular size will reveal the size of the area of chemical infiltration around the disc. If an organism is put on the agar it will not grow in the area around the disc if it is susceptible to the chemical. This area of no growth around the disc is known for example a zone of inhibition or Clear zone. Designed for the disc diffusion, the zone diameters were measured through slipping calipers of the National Committee pro Clinical Laboratory Standards. Agar-based methods for example E-test and disk diffusion can be well alternatives for the reason that they are easier and further rapidly than broth-based methods [6].

2.6.2 Anticancer activity

Probable cytotoxicity of the compounds was tested using the method of Skehan and Storeng [7]. Cells were plated into 96-multi properly plate (104 cells/well) for 24 hr before treatments via the compounds to allow attachment of cell to the wall of the plate various dilutions of the compounds beneath analysis (0, 5, 12.5, 25, 50 and 100 µg/ml) were intermixed to the cell monolayer. The monolayer cells were reserved warm including the compounds for 48 h at 37 ºC and within 5% CO_2 atmosphere. After 48 h, cells were fixed, washed and stained by SRB stain. Excess stain was washed using acetic acid also attached stain was convalesced by Tris-EDTA buffer. The optical density (O.D.) of every one good was measured spectrophotometrically at 564

nm via an ELIZA microplate reader, the average background absorbance was automatically subtracted, in addition to mean values of each drug concentration were calculated. The relation between drug concentration plus surviving fraction is plotted to become the survival curve of breast tumor cell line for each compound. The percentage of cell survival was calculated as follows:

Survival fraction = O.D (treated cells)/O.D (control cells)

The IC_{50} values (the concentrations of the Schiff base ligand (L) or its metal complexes required to produce 50% inhibition of cell growth) [6].

2.6.3 Computational methodology

Gaussian09 suite of program was designed for the electronic structure calculations for H_2L and Cd(II) complex. DFT based B3LYP method along by the LANL2DZ basis regulate was employed for full optimization. In order to assimilate the effect of the solvent around the molecule, the TDDFT method (along with LANL2DZ basic set) was used to calculate the electronic absorption spectra of the ligand and its Cd(II) complex.

2.6.4 Molecular docking

In order to expose the possible binding modes of the most excellent active compounds opposed to the crystal structure of the SARS-CoV-2 (COVID-19) main protease in complex with inhibitor UAW247 (PDB ID: 6XBH), molecular docking studies were performed using MOE2008 software. It is a stiff molecular docking software and is a communicating molecular graphics program in provide for calculating in addition displaying possible docking modes of a receptor and ligand and complexes molecule. It requires the ligand and the receptor like input in PDB format. The amino acid sequence was reserved and the crystallized ligands, water molecules and chloride ions in out sphere were deleted. Crystal structure of the SARS-CoV-2 (COVID-19) was downloaded from the protein data bank (http://www.rcsb.org./pdb) [8].

3. Results and discussion

3.1 Schiff base characterization

The novel Schiff base, H_2L, is subjected to elemental analyses. The outcome of elemental analyses (N, H and C) by molecular formula in addition to the melting point are existing in Table 1. The results obtained are in well agreement using those calculated from the suggested formula. The melting points are sharp representing the purity of the preparation Schiff base. The scheme of the Schiff base preparation is given in Scheme1. The structure of this Schiff base is additionally confirmed via IR and ^1H NMR spectra, which will be discussed in detailed together with its metal complexes later [9].

3.2 Composition and structure of Schiff base and its complexes

3.2.1 Elemental analysis

The novel Schiff base ligand was an orange solid and stable at 37 ℃. It was soluble in DMF. The results obtained were in well-behaved agreement via those calculated from the suggested formula. The structure of the Schiff base ligand under study was exposed in Figure 1.

As supposed as a result of the elemental analyses data (Table 1), the metal/ligand ratio was found to be 1:1 in all complexes, which have been arrived on account of estimating the carbon, hydrogen, nitrogen and metal contents of the complexes. The metal complexes had the composition of MH_2L type. The results of the experimental elemental analysis of H_2L and its complexes had compactly values near the theoretical calculations (Table 1) [10].

3.2.2 Infrared spectra

The IR spectra of the ligand in addition to its complexes showed a broad band at 3165–3439 cm^{-1} which may be assigned to ν(OH) phenolic and ν(OH) vibration modes of water molecules. The coordinated water molecules generally showed characteristic peaks nearly 750 cm^{-1} attributable to ρr(H_2O) and 650 cm^{-1} attributable to ρw(H_2O). Nevertheless, the presence of different types of water molecules may be confirmed further through TG-DTG analysis [11, 12]. H_2L ligand showed a lack of the NH_2 stretching band characteristic of 4-aminoantipyrine. Alternatively, a new strong and sharp vibration band was appeared at 1589 cm^{-1} attributable to the azomethine group, ν(C═N), indicating the formation of the Schiff base product (H_2L). IR spectra of the complexes exhibited shifts in the band related to the azomethine groups, ν(C═N) which refers to the coordination of this group to the metal ions [14]. The broad band of carbonyl, ν(C═O), groups of resorcinol and 4-aminoantipyrine was appeared at 1652 cm^{-1} [13]. The complexes showed bands at 1626-1652 and 1595-1636 cm^{-1} which were assigned to carbonyl group of resorcinol and antipyrine, respectively. The small shift in peak site of the carbonyl group of resorcinol can be accounted to the hydrogen bond formation through the neighboring hydrogen. The high shift in peak site of the carbonyl group of antipyrine can be assigned to its involvement in coordination to metal ions. This was confirmed by the appearance of new low intensity bands at lower wavenumbers corresponding to stretching vibrations of M-N bond in the region 421–459 $cm^{-1}$and M-O bond in the region of 546–599 cm^{-1} [14]. The data of the IR spectra of Schiff base ligand (H_2L) and its mononuclear metal complexes were listed in Table (2) [6].

3.2.3 ^{1}H NMR spectral study

^{1}H NMR spectral data (δ ppm) of the free ligand in relation to TMS (0 ppm) in DMSO-*d*$_6$ were obtained to support the ligand structure in addition to its purity. The signals observed at 16.10 and 16.73 ppm can be assigned to two phenolic OH_a and OH_b protons, respectively. The spectrum of free ligand (H_2L) exhibited a multiple signal at 6.27-8.41ppm region, which can be assigned to aromatic region, (m,7H, Ar-H). In the aliphatic region, the ligand spectrum showed overlapping singlet signals observed at 2.26-3.13 ppm assigned to methyl protons (s, 12H, $4CH_3$) [6, 11, 15]. The absence of peak at around 4 ppm assigned to $–NH_2$ group indicated most wanted product formation [16].

^{1}H NMR spectral (δ ppm) information of Cd(II) and Zn(II) complexes showed phenolic OH_a and OH_b protons at 16.10 and 16.67 ppm and 16.11 and 16.70 ppm, respectively. The phenolic OH_b proton was slightly shifted from its position in the free ligand which indicated that OH_b participated in coordination to the metal ions without proton displacement. While, the phenolic OH_a proton appeared in the same position of the free ligand confirming its non-involvement in chelate formation. In the aromatic region, benzene showed overlapping signals observed at the range of 6.27-8.40 and 6.27-8.38 ppm for Zn(II) and Cd(II) complexes, respectively. The methyl protons were found in the aliphatic region (m, 12H, $4CH_3$) as overlapping singlet signals observed in the range 2.10-3.50 and 2.09-3.31 ppm for Cd(II) and Zn(II) complexes, respectively [17].

3.2.4 Molar conductivity measurement

The molar conductivity of the metal complexes was measured inside DMF as solvent (Table 1). Their molar conductivity measurements in DMF were found in the range of 9-113 $ohm^{-1}cm^2mol^{-1}$. The molar conductance values of the complexes indicated that they were electrolytic in nature except Zn(II) and Cd(II) complexes which are non-electrolytes as found from their molar conductance values [18].

3.2.5 Electronic spectra and magnetic properties of prepared complexes

The magnetic susceptibility measurements in addition to electronic spectral data have been used to invest the structure of complexes. The effective magnetic moment (μ_{eff}) values have been experimentally measured at room temperature (300 K) and used for predicting the geometry of the complexes. The electronic spectra of ligand and its metal complexes measured in DMSO solutions within the wavelengths range 200–700 nm. The UV-Vis spectrum of the solution of prepared ligand reveals only one high-intensity peak at 395 nm assigned to n→π* transition. This peak shifted in the spectra of complexes to lower wavelengths, upon the coordination of the ligand. The spectra of Cr(III), Mn(II), Fe(III), Ni(II), Cu(II), Zn(II) and Cd(II) complexes showed peaks in the range of 337-378 nm related to n→π* transition [19].

Chromium(III) complex showed magnetic moment equivalent to three unpaired electrons, i.e. 3.99 B.M., predictable for high-spin octahedral chromium(III) complexes. Six coordinated Cr(III) complex, as well as octahedral geometry showed three spins allowed bands in the range of 18,000–30,000 cm^{-1} [19, 20]. The Cr(III) complex displays bands at 17,953, 25,169, 26,436, and 39,525 cm^{-1}, respectively. These bands may be ascribed to $^4B_{1g} \rightarrow {}^4E_g$, $^4B_{1g} \rightarrow {}^4B_{2g}$, $^4B_{1g} \rightarrow {}^4Eb_g$ and $^4B_{1g} \rightarrow {}^4A_{1g}$ transitions, respectively, resulting from the lifting of the degeneracy of the orbital triplet (in octahedral) in the order of increasing energy [19, 20].

Manganese(II) complex showed magnetic moment equivalent to five unpaired electrons, i.e. 5.41 B.M., supposed for high-spin octahedral manganese(II) complexes. The Mn(II) complex displays bands at 17801, 21,942 and 24,492 cm^{-1}, respectively. These bands may be ascribed to $^6A_{1g} \rightarrow {}^4T_{1g}(G)$; $^6A_{1g} \rightarrow {}^4T_{2g}(G)$ and $^6A_{1g} \rightarrow {}^4T_{1g}(P)$ transitions, respectively. Thus the ligand field bands and magnetic moment value support an octahedral geometry around manganese(II) ion [6, 21].

Iron(III) complex showed magnetic moment corresponding to three unpaired electrons, i.e. 5.28 B.M., supposed for high-spin octahedral Iron(III) complexes [6]. Six coordinated Fe(III) complexes with octahedral showed three bands at 22,127, 19,897 and 17,035 cm^{-1}, respectively. These bands may be ascribed to $^4T_{2g}(G) \rightarrow {}^6A_{1g}$, $^4T_{2g}(G) \rightarrow {}^6A_{1g}$ and $^4T_{1g}(D) \rightarrow {}^6A_{1g}$ transitions, respectively, indicating the octahedral geometry of the complex [6].

The nickel(II) complex showed magnetic moment value of 4.39 B.M. equivalent to two unpaired electrons. Electronic spectrum displayed bands at 12,219, 17,002 and 23,122 cm^{-1}. These bands may be ascribed to $^3A_2(F) \rightarrow {}^3T_2(F)$, $^3A_2(F) \rightarrow {}^3T_1(F)$ and $^3A_2(F) \rightarrow {}^3T_1(P)$ transitions, respectively. It suggests tetrahedral geometry of Ni(II) complex [20]. Usually, square planar Ni(II) complexes are diamagnetic while tetrahedral complexes have magnetic moments in the range of 3.2–4.1 BM. The Ni(II) complex reported here at a room temperature magnetic moment value of 3.33 BM (Table 1), which is within the normal range observed for tetrahedral Ni(II) complex [22].

Electronic spectrum of the copper(II) complex displays bands at 10842, 19,765 and 29,928 cm^{-1}. First two bands may be ascribed to the transitions: $^2B_{1g} \rightarrow {}^2A_{1g}$ ($dx^2-y^2 \rightarrow dz^2$) and $^2B_{1g} \rightarrow {}^2B_{2g}$ ($dx^2-y^2 \rightarrow dzy$), respectively. the third band may be due to charge transfer. Also, the magnetic moment value of the copper(II) complex is 2.80 B.M. which equivalent to the presence of one unpaired of electron which is consistent with tetrahedral geometry. This indicated the formation of tetrahedral geometry of the complex [6, 20, 22, 23].

Generally, Zn(II) and Cd(II) complexes were suggested to have octahedral geometry and they did not exhibit any d–d electronic transition due to its completely filled d^{10} orbital [6, 22].

3.2.6 Geometry optimization

The completely optimized geometries of the ligand H_2L plus its Cd(II) complex were shown in Figure1. The values of the chosen bond lengths and bond angles calculated for Cd(II) complex showed distorted octahedral geometry around the Cd(II) ion (Table 3). A little elongation in bond lengths C(25) - N(26), C(1) - O(24) and C(29) - O(40) were found to be 1.50, 1.33 and 1.45 A°, respectively. That was noted in Cd(II) complex as ligand H_2L coordinated through azomethine nitrogen, oxygen of the carbonyl and phenolic oxygen while another three positions were occupied by two chloride ions and oxygen of coordinated water. The bond angles in the coordination sphere of Cd(II) complex were investigative of octahedral geometry, as previously indicated. The reduce in the metal-chloride angles can be ascribed to intramolecular hydrogen bond [6].

3.2.6.1 Molecular electrostatic potential (MEP)

With the aim of study, the reactions, electrostatic potential V(r) maps were calculated which are used for the recognition of the electronic charge distribution around molecular surface and consequently to expect sites for the reactions. These maps were calculated by using the equal basis put like for optimization. In the existing study, 3D plots of MEP were drawn for the ligand and its Cd(II) complex. Based on the MEP, one can usually order the electron-rich area which has red color on the map (a preference position for electrophilic attack). Nevertheless, the electron-poor region has a blue color (a preference position for nucleophilic attack). But the region with green color points to the neutral electrostatic potential region. It can be seen that the H_2L is stable having a practically uniform distribution of charge density. Nevertheless, two oxygen and nitrogen atoms are surrounded by a greater negative charge surface, making these sites potentially extra favorable for electrophilic attack (red) (Figure 2) [6].

The aromatic ring seems neutral in conditions of electron density. As a result the distribution of potential is in favor of the complexation reaction which is further confirmed via the electrostatic potential distribution of Cd(II) complex, where a greater negative charge is surrounded to the metal center (Figure 2b). The Mulliken electronegativity additionally indicated the rise of the electronegativity of oxygen and nitrogen in Cd(II) complex than free H_2L making them the favor site of electrophilic attack with metal ion [6].

3.2.6.2 Molecular parameters

Additional parameters such as the highest occupied molecular orbital energy (E_{HOMO}), the lowest unoccupied molecular orbital energy (E_{LUMO}), ΔE, absolute electronegativities, χ, chemical potentials, Pi, absolute hardness, η, absolute softness, σ, global electrophilicity, ω, global softness, S, and additional electronic charge, ΔN_{max} have been estimated for the H_2L free ligand and its Cd(II) complex and listed in Table 3. Electrophilicity index (ω) is one of the most important quantum chemical descriptors in describing toxicity and the reactivity of various selective sites. The electrophilicity may quantify the biological activity of drug receptor interaction. Also, this index measures the stabilization energy when the system acquires extra negative charge from the environment. η and σ indexes, are the measure of the molecular stability and reactivity also, their concepts are related to each other. The softness indexes are the vice versa image for global hardness. These parameters are useful in order to support the suggestion structures. The mentioned quantum chemical parameters were calculated with the help of the following equations:

$$\Delta E = E_{LUMO} - E_{HOM} \quad (1)$$

$$\chi = \frac{-(E_{HOMO} + E_{LUMO})}{2} \quad (2)$$

$$\eta = \frac{E_{LUMO} - E_{HOMO}}{2} \quad (3)$$

$$\sigma = \frac{1}{\eta} \quad (4)$$

$$Pi = -\chi \quad (5)$$

$$S = \frac{1}{2\eta} \quad (6)$$

$$\omega = \frac{Pi^2}{2\eta} \quad (7)$$

$$\Delta N_{max} = \frac{Pi}{\eta} \quad (8)$$

The data calculated were presented in Table 3 and reflected the following notes:

i) The data of H_2L and its Cd(II) complex had a great chance and priority for biological activity based on high ω value.

ii) S and □ were the softness indexes while η are for hardness indication; a hard molecule had a high stability due to its high energy difference in-between the E_{HOMO} and E_{LUMO} than the soft

molecule. So, the soft molecule was the reactive one having flexible donation towards the metal ions. Accordingly, the investigated H_2L molecule was soft towards the coordination.

iii) The positive electrophilicity index (χ) value and the negative electronic chemical potential (μ) value indicated that the H_2L molecule capable of accepting electrons from the environment and its energy must decrease upon accepting electronic charge. Therefore, the electronic chemical potential must be negative.

iv) The Cd(II) complex showed high values of dipole moments than the free ligand.

Both the highest occupied molecular orbital (HOMO) and lowest unoccupied molecular orbital (LUMO) were the main orbitals that participate in chemical stability. The HOMO represents the ability to donate an electron, LUMO as an electron acceptor represents the ability to obtain an electron. From the attained data, it can assume that:

1. The energies of the HOMO and LUMO were negative values and more negative than free H_2L, which showed the stability of isolated complex.
2. The E_{HOMO} and E_{LUMO} values of Cd(II) complex were calculated and showed a decrease than the free ligand which represents the strength of M–H_2L shorter bonds.
3. The total energy of Cd(II) complex was higher than free ligand, which indicated greatly the stability of the isolated solid complex.
4. The small energy gap can be associated with a high chemical reactivity, low kinetic stability and reflects to efficient electronic charge transfer interaction making the molecule highly polarizable.
5. The HOMO level was mostly localized on the azomethine nitrogen and oxygen of phenol group in the ligand, which indicated the preferable sites for nucleophilic attack to the central metal atom [4, 6]. Table 3. The different optimized and quantum chemical parameters of H_2L and its Cd(II) complex.

3.2.6.3 UV-Vis spectra

An understanding of the photochemistry of transition metal compounds requires knowledge of the properties of molecular orbitals and appropriate excited states. Frontier orbitals played a relevant role in such systems, because they rule the electronic excitations and the transition characters. With the aid of TD-DFT calculations, it is possible to have comments about the contributions of the ligand and metal orbitals to molecular orbitals. It is not practical to analyze all the electronic transitions and the orbitals; therefore, some restrictions were used. Due to high accuracy and low computational cost of TD-DFT, it has been popularized for theoretical investigation of electronic spectra of molecules. The present investigation for low laying excited state on optimized ground state structures of H_2L and its Cd(II) complex have been performed at TD-DFT/B3LYP/ LANL2DZ level of theory for thirty singlet state. In Table 6, the experimental

and theoretical electronic spectra were presented. The TD-DFT calculations have been evaluated in the N,N-dimethylformamide solvent background and compared with the experimental data. The transitions between interfrontier orbitals for wavelengths corresponding to maximum oscillator strength of simulated results with contemporary experimental observations were presented in Figure (3a, b). For example, the electronic transitions for H_2L obtained at calculated 366 nm correspond to experimental peak at 395 nm. This transition has been majorly contributed from HOMO to LUMO+2 transitions which was primarily $\pi \rightarrow \pi^*$ in nature. The different transitions and its experimental counterpart of the free ligand and its Cd(II) complex have been summarized in Table 4 [4, 6].

3.2.7 Thermogravimetric Analysis

TG and DTG analysis outcome of H_2L and its metal complexes at a heating rate of 10 °C/min in nitrogen atmosphere over the range from 30 to 1000 °C were summarized in Table (5).

The Schiff base ligand with the molecular formula ($C_{21}H_{21}N_3O_4$) was thermally decomposed in three successive decomposition steps, within the range from 30 to 900 °C via total mass loss of 97.69 % (calcd.= 100%). The first and second stages in the temperature range of 30 – 330 °C were correlated through evolution of $C_{10}H_{21}$ molecule including mass loss of 37.69% (calcd.= 37.25%) per a maximum at 195 and 255 °C. The last stage in the temperature range of 330–900 °C was correlated through evolution of $C_{11}N_3O_4$ molecule including mass loss of 60.17 % (calcd.= 62.75%) per maximum at 400 °C.

The $[Cr(H_2L)(H_2O)_2Cl]Cl_2.2H_2O$ complex showed four decomposition stages in the range from 30 to 900 °C including total mass loss of 75.34 % (calcd.= 77.21%) leaving $½Cr_2O_3$ contaminated by carbon atoms as residue. The first stage in the temperature range of 30–120 °C was correlated through evolution of two uncoordinated water molecules including mass loss of 5.64 % (calcd.= 5.90%) per a maximum at 66 °C. The last three stages in the temperature range of 120-900 °C were correlated through evolution of two water molecules, $3/2Cl_2$ and $C_{16}H_{22}N_3O_{2.5}$ molecule and through mass loss of 69.70% (calcd.=71.31%) per maximum at 218, 700 and 810 °C.

The $[Mn(H_2L)(H_2O)_2Cl]Cl.2H_2O$ complex showed five decomposition stages in the range from 30 to 900 °C including total mass loss of 76.12% (calcd.= 77.24%) leaving MnO contaminated by carbon atoms as residue. The first three stages within the temperature range of 30 –375 °C were correlated through evolution of four water molecules, Cl_2 and C_4H_{10} molecule including mass loss of 34.50% (calcd.= 34.81%) per a maximum at 71, 125 and 155 °C. The last two stages in the temperature range of 375-900 °C were correlated through evolution of $C_{12}H_{11}N_3O_3$ molecule via mass loss of 41.62% (calculated mass loss = 42.43%) per two maximum at 379 and 812 °C.

The $[Fe(H_2L)(H_2O)_2Cl]Cl_2$ complex showed two decomposition stages within the range from 30 to 900 °C including total mass loss of 78.15 % (calcd.= 77.78%) leaving ½Fe_2O_3 contaminated by carbon atoms as residue. The first and second stages within the temperature range of 30–900 °C were correlated through evolution of $5H_2O$, Cl_2 and $C_{17}H_{21}N_3O_{2.5}$ molecules including mass loss of 78.15% (calcd.= 77.78%) per a maximum at 139 and 204 °C.

The $[Ni(H_2L)(H_2O)]Cl_2.4H_2O$ complex showed four decomposition stages within the range from 30 to 900 °C including total mass loss of 78.20 % (calcd.= 77.61%) leaving NiO contaminated by carbon atoms as residue. The first two stages within the temperature range of 30–250 °C were correlated with evolution of $5H_2O$ and Cl_2 uncoordinated molecules including mass loss of 27.29% (calculated mass loss = 26.87%) per a maximum at 73 and 157 °C. The last two stages within the temperature range of 250–900 °C were correlated through evolution of $C_{16}H_{21}N_3O_3$ molecules including mass loss of 50.91% (calcd.= 50.74%) per a maximum at 183 and 424 °C.

The $[Cu(H_2L)Cl]Cl.2H_2O$ complex showed four decomposition stages within the range from 30 to 900 °C including total mass loss of 75.58% (calcd.= 76.74%) leaving CuO and carbon atoms as residue. The first stage within the temperature range of 30–135 °C was correlated through evolution of $2H_2O$ uncoordinated molecules including mass loss of 6.56% (calcd.= 6.55 %) per a maximum at 68 °C. The last three stages within the temperature range of 135–900 °C were correlated through evolution of Cl_2 and $C_{17}H_{21}N_3O_3$ molecules, including mass loss of 69.02% (calcd.=70.19%) per a maximum at 169, 270 and 550 °C.

The $[Zn(H_2L)(H_2O)Cl_2]2H_2O$ complex showed six decomposition stages within the range from 30 to 900 °C including total mass loss of 72.68% (calcd.= 73.02%) leaving ZnO and carbon atoms as residue. The first two stages within the temperature range of 30–180 °C were correlated through evolution of $3H_2O$ molecules including mass loss of 9.47% (calcd.= 9.48%) per a maximum at 61 and 155 °C. The next two stages within the temperature range of 180–365 °C were correlated through evolution of Cl_2 and $3CH_4$ molecules including mass loss of 19.77% (calcd.= 20.89%) per a maximum at 178 and 285°C. The last two stages within the temperature range of 365–900 °C were correlated through evolution of $C_{12}H_{19}N_3O_3$ molecule, including mass loss of 43.44% (calcd.= 42.65%) per a maximum at 464 and 800 °C.

The $[Cd(H_2L)(H_2O)Cl_2]$ complex showed five decomposition stages within the range from 30 to 900 °C including total mass loss of 73.48% (calcd.= 71.80%) leaving CdO and carbon atoms as residue. The first stage within the temperature range of 30–160 °C was correlated through evolution of H_2O molecules including mass loss of 3.65% (calcd.= 3.10%) per a maximum at 132 °C. The second stage within the temperature range of 160–245 °C was correlated through evolution of Cl_2 molecule including mass loss of 11.83% (calcd.= 12.22%) per a maximum at 217 °C. The third stage within the temperature range of 245–480 °C was correlated through

evolution of $C_{10}H_{21}$ molecule, including mass loss of 24.70% (calcd.= 24.45%) per a maximum at 268°C. The last two stages within the temperature range of 480–900 °C were correlated through evolution of $C_7N_3O_3$ molecule, including mass loss of 33.30% (calcd.= 32.03%) per a maximum at 561 and 833 °C.

The thermogram of the complexes inveterate their structures where the presence of uncoordinated water molecules in all metal complexes but Cd(II) complex was suggested and all complexes had octahedral geometry except Ni(II) and Cu(II) complexes have tetrahedral geometry.

3.2.8 Mass spectral study

The mass spectrum of H_2L ligand exhibited a molecular ion peak at m/z = 379 amu matching to $[M]^+$, which proven the proposed formula $[C_{21}H_{21}N_3O_4]^+$. The intensity of these peaks gave an idea of calculating value 379.43 amu.

The mass spectrum of Cd(II) complex revealed a molecular ion peak at m/z = 580.5 amu which was coextensive via the calculated weight of 580.8 amu. This result proven the stoichiometry of this complex as being of $[MH_2L]$ type. On the other hand, the peak of the parent ligand in the mass spectrum of the Cd(II) complex seemed at m/z 379 amu. The full-scan mass spectra of ligand and Cd(II) complex were shown in Figure 4 [6].

3.2.9 Structural interpretation

The structures of the metal complexes of the tridentate Schiff base ligand (H_2L) were characterized through elemental analyses, molar conductivity, IR, ^{1}HNMR, UV–Vis, mass and thermal analyses after that the suggested structures of transition metal complexes were given in Figure 5.

3.2.10 BET surface area

The BET measurements (Table 6) were carried out in the direction of determine the surface area of the metal complexes. The obtained data showed high surface area, which were found in the range of 23–176 $m^2\ g^{-1}$. It is to be observed that the high surface area, might be contributed to the mesoporous structure and nano size of the particles with average particle radius of 4.32- 8.71nm [24]. Surface area and pore volume values estimated through nitrogen adsorption isotherms by relative pressures (p/p^o) are given inside Table 3. The micro pore volumes and S_{BET} values of entrapped complexes showed an excessively large decrease in pore volume (0.33–0.02 cc/g) and surface area (200–13 m^2/g) [25].

3.2.11 Antimicrobial assays

An *in-vitro* antibacterial activity outcome of the Schiff base plus metal complexes were tested opposed to the one Gram-negative (*Escherichia coli*) and the one Gram-positive (*Staphylococcus aureus*) bacterial strains and *in vitro* antifungal activity results opposed to *C. albicans* and *A. flavus* through well diffusion method [26]. The results are shown in Table 7.

A relative study of the Schiff base and its complexes showed that metal complexes reveal higher antimicrobial activity than the Schiff base (Figure 6). This is because of the reduction in size of metal chelates upon coordination of ligand which enhance the lipophilicity of complexes and for this reason, diffusion of metal ion through cell membrane becomes leisurelier. Thus, chelating effect makes the metal complex like strong antibacterial agents and so inhibits the growth of microorganisms or destroys the microbes as a result of blocking their active sites [26, 27].

The behavior of the prepared Schiff base ligand and its metal complexes were validated through calculating the activity index consistent in addition to the following relation and that showed in Figure 7 (a,b).

Activity index (A) = Inhibition Zone of compound mm /Inhibition Zone of standard drug mm ×100.

Lastly, the order of rising bacterial and fungal growth inhibitory capacity is in the following order:

For *E. coli*: Cr(III)<Mn(II)<Fe(III)<H_2L=Zn(II)=Cu(II)< Ni(II)< Cd(II),

For S. aureus: Cr(III)<Mn(II)<Fe(III)<H_2L< Zn(II)=Cu(II)< Ni(II)< Cd(II),

For *Candida albicans*: H_2L=Zn(II)< Fe(III)< Ni(II)< Cd (II)

and For *Aspergillus flavus* Cd(II)< Fe(III).

End result improves that, the higher antimicrobial activity by ligand bound complexes than the free ligand compared using antibiotics. In addition, in the metal complex, the maximum zones were obtained in iron(III) complex with 14 mm zone of inhibition against *E. coli*, Cadmium(II) complex with 20 mm in *S. aureus*, Cadmium(II) complex with 24, 20 mm in *Aspergillus flavus* and *Candida albicans,* respectively [28].

Just before assess the biological profile, an additional series of antimicrobial agents based on metals by a [(1E)-1-(2-hydroxyphenyl)ethylidene]-2-oxo-2H-chromene- 3-carbohydrazide SB is possessing a NOO donor structure was synthesized and in detail analyzed. Cd(II) complex showed the maximum zone of inhibition (18 and 20 mm) of *E. coli* and *Staphylococcus aureus* cells compared to reported [Cd(H_2L)(H_2O)Cl_2] complex whcih showed the maximum zone of inhibition (24 and 20 mm) [29, 30].

For the same SB, Fe(III) complex showed the maximum zone of inhibition (14 mm) against *Aspergillus flavus* which is the same to reported [Fe(H_2L)(H_2O)$_2$Cl]Cl_2 which showed the maximum zone of inhibition (14 mm) [31].

Also, another series of antimicrobial agents based on metal ions with 2-(((1,5-dimethyl3-oxo-2-phenyl-2,3-dihydro-1H-pyrazol-4-yl)imino) (phenyl)methyl)benzoic acid SB, Cd(II) complex showed the maximum zone of inhibition (20 mm) against *Candida albicans* which is similar to the reported [Cd(H_2L)(H_2O)Cl_2] complex (maximum zone of inhibition 20 mm) [4].

This top antimicrobial activity of the metal complexes compared to Schiff base and the disparity in activity arise from the different nature of the metal ions and their coordination modes. Chelation reduces the polarity of the metal ion and improves the lipophilicity of the metal complex and, between all the tested complexes, the complete rupture of the cells depicted that the complex bound to the cell wall and ruptured it caused by oxidative stress on microbial cell, entering into the nucleus, thus degrading the chromosomal DNA through preventing protein synthesis which is necessary for all cellular metabolism [29].

3.2.12 Anticancer effects of Schiff base and its complexes

The novel Schiff base ligand in addition to its complexes have been tested for their anticancer effect on the human breast cancer cell line (MCF-7) through several concentrations. The anticancer activity outcomes of the compounds at 100 μg/ml were explained within Table 8. The % cell inhibition and IC_{50} values were found out and implies that copper complex has higher sensitivity towards the breast cancer lines than the free ligand and other complexes inside Figure 8 [26].

The *in vitro* biological test analysis outcome revealed that metal complexes have higher biological activity than the Schiff base. The better activities of the metal complexes are due to the effect of metal ions on the normal cell membrane. Additionally, chelation enhances the biochemical potential of bioactive Schiff base through modifying hydrophilicity and lipophilicity which brings down the permeability barriers of cell and manage the rate of entry of molecules into the cell wall. This type of effect increases the penetration of the metal complexes into lipid membranes and overcrowding of the metal binding sites in the enzymes of microorganisms. Additionally, it distracts the respiration process of the cell and correspondingly blockades the synthesis of the proteins that restricts supplementary growth of the organisms [26].

Comparing the IC_{50} values of Mn(II), Fe(III), Ni(II) and Cu(II) complexes, it can be found that the Cu(II) has stronger activity in opposition to human breast cancer cell line (MCF-7) than the other complexes, and its IC_{50} value is 19.6 mg/L, and the IC_{50} value of cisplatin is 14.52 mg/L, the greatest anti-human breast cancer cell MCF-7 activity. At this time, the IC_{50} value of cisplatin is more than 100 mg/L. These results give more possibilities in support of the research and development of metal anticancer drugs and provide some experimental data for the development and application of organotin anticancer drugs. Other than their performance should be further studied [32].

3.2.13 Molecular modeling: Docking study

Molecular docking studies have been carried out with the purpose of imagine the binding modes of the H_2L ligand and its metal complexes to crystal structure of the SARS-CoV-2 (COVID-19) main protease in complex by inhibitor UAW247 (6XBH). The lesser most binding energies of

the ligand and its metal complexes by 6XBH were calculated and showed in Figure 10. 3D interaction maps showed the binding models of H_2L and its metal complexes toward protein. It was confirmed that wholly the tested compounds were interacted via a hydrogen bond (Table 9) and Figure 9.

After analyzing the out of 8 predicted binding conformations of ligand, Cr(III), Mn(II), Fe(III), Ni(II), Cu(II), Zn(II) and Cd(II) complexes with 6XBH dockings, the most excellent confirmations exhibited that the free energies of binding (ΔG) were -2.5, -28.6, -3.3, -5.0, -4.9, -3.0, -8.0 and -6.5 kcal/mol, respectively. Ligand, Cr(III), Fe(III) and Ni(II) complexes are binding via H-donor except Mn(II), Cu(II), Zn(II) and Cd(II) are binding by H-acceptor with 2.88, 3.38, 3.77, 2.86, 3.31, 3.08, 3.06 and 3.34 A° distances, respectively [33, 34].

The values of interaction energies revealed that its Cr(III) complex had the greatly stable interaction has a lesser binding energy. Since the point of view of binding energy, shows strong interactions with the targets of new coronavirus [3, 6].

4. Conclusion

Novel tridentate NOO type Schiff base and Cr(III), Mn(II), Fe(III), Ni(II), Cu(II), Zn(II) and Cd(II) complexes were synthesized and characterized. Full recognized structural features of the synthesized compounds were done as a result of elemental analysis, molar conductance, magnetic susceptibility, ^{1}H-NMR, FTIR and UV-Vis spectral techniques. IR and ^{1}H NMR and UV-vis spectral studies indicated the tridentate nature of the ligand and its coordination through one azomethine nitrogen and two oxygen atoms for all complexes. Magnetic moments and UV-vis spectral studies suggested octahedral geometry of Cr(III), Mn(II), Fe(III), Zn(II) and Cd(II) complexes and tetrahedral geometry for Ni(II) and Cu(II) complexes. In addition, structural characterization shows the larger surface area and small pore size of the BET result. It can be used in various nanotechnology applications.

Generally, beginning the activities of the novel metal complexes as pathogenic of microorganism, the metal complexes displayed extra antimicrobial activities than the free ligand molecules. H_2L was successful to fight against the recent coronavirus. Its Cr(III) complex with a lower binding energy than the ligand of the crystal structure, which suggests a possible strong antiviral activity. This research will conduce to the treatment against new coronavirus.

References:

1. More MS, Joshi PG, Mishra YK, Khanna PK. Metal complexes driven from Schiff bases and semicarbazones for biomedical and allied applications: a review. Mater Today Chem [Internet]. 2019;14:100195. Available from: https://doi.org/10.1016/j.mtchem.2019.100195
2. Ommenya FK, Nyawade EA, Andala DM, Kinyua J. Synthesis, Characterization and Antibacterial Activity of Schiff Base, 4-Chloro-2-{(E)-[(4-Fluorophenyl)imino]methyl}phenol Metal (II) Complexes. J Chem. 2020;2020.
3. Yu R, Chen L, Lan R, Shen R, Li P. Computational screening of antagonists against the SARS-CoV-2 (COVID-19) coronavirus by molecular docking. Int J Antimicrob Agents [Internet]. 2020;2:106012. Available from: https://doi.org/10.1016/j.ijantimicag.2020.106012
4. Mahmoud WH, Deghadi RG, Mohamed GG. Preparation, geometric structure, molecular docking thermal and spectroscopic characterization of novel Schiff base ligand and its metal chelates: Screening their anticancer and antimicrobial activities. J Therm Anal Calorim. 2017;127(3):2149–71.
5. Bauer AW, Kirby WM, Sherris JC, Turck M. Antibiotic susceptibility testing by a standardized single disk method. Am J Clin Pathol. 1966;
6. Mahmoud WH, Omar MM, Ahmed YM, Mohamed GG. Transition metal complexes of Schiff base ligand based on 4,6-diacetyl resorcinol. Appl Organomet Chem. 2020;34(4):1–20.
7. P. Skehan, R. Storeng. J. Natl. Cancer Inst. 82 (1990) 1107- 1112
8. Zhang J. Molecular dynamics studies on the COVID-19 main protease dimer (with unliganded active site / without ligand) and the COVID-19 nsp15 endoribonuclease (in the complex with a citrate ... 2020;(June).
9. Abdallah SM, Zayed MA, Mohamed GG. Synthesis and spectroscopic characterization of new tetradentate Schiff base and its coordination compounds of NOON donor atoms and their antibacterial and antifungal activity. Arab J Chem. 2010;3(2):103–13.
10. Mahmoud WH, Mahmoud NF, Mohamed GG, El-Bindary AA, El-Sonbati AZ. upramolecular structural, thermal properties and biological activity of 3-(2-methoxyphenoxy)propane-1,2-diol metal complexes. J Mol Struct [Internet]. 2015;1086:266–75. Available from: http://dx.doi.org/10.1016/j.molstruc.2015.01.003
11. Shebl M, El-Ghamry MA, Khalil SME, Kishk MAA. Mono- and binuclear copper(II) complexes of new hydrazone ligands derived from 4,6-diacetylresorcinol: Synthesis, spectral studies and antimicrobial activity. Spectrochim Acta - Part A Mol Biomol Spectrosc

[Internet]. 2014;126:232–41. Available from: http://dx.doi.org/10.1016/j.saa.2014.02.014

12. Mariana loredana dianu1*, angela kriza1 ns, musuc2 and am. Transition metal M(II) complexes with isonicotinic acid 2-(9-anthrylmethylene)-hydrazide. 2010;75(11):1515–31.
13. Mahmoud WH, Mahmoud NF, Mohamed GG. Spectroscopic characterization and molecular docking studies of acetyl ferrocene-derived Schiff base ligand with phenanthroline and some transition metal ions. J Therm Anal Calorim. 2017;
14. Abdulghani AJ, Hussain RK. Synthesis and Characterization of Schiff Base Metal Complexes Derived from Cefotaxime with 1 H -indole-2 , 3-dione (Isatin) and. 2015;(October):83–101.
15. Emara AAA, Adly OMI. Synthesis and Spectroscopic Studies of new binuclear transition metal complexes of Schiff bases derived from 4,6-diacetylresorcinol. Transit Met Chem. 2007;32(7):889–901.
16. Surve RR, Sankpal ST. synthesis of new sulphanilamide based schiff base nickel complexes with study of its antibacterial activity and nanoparticle. 2020;13(1):282–90.
17. Mahmoud WH, Mahmoud NF, Mohamed GG, El-bindary AA, El-sonbati AZ. Supramolecular structural, thermal properties and biological activity of 3-(2-methoxyphenoxy)propane-1,2-diol metal complexes. J Mol Struct [Internet]. 2015; Available from: http://dx.doi.org/10.1016/j.molstruc.2015.01.003
18. Ramarasan S, Sharma LR, Angelo ANP. synthesis , spectral characterization and antimicrobial studies of Co(III), Ni(II), Cu(II) and Zn(II) metal complexes of schiff base derived from 4 , 6-diacetyl resorcinol and 4-chloro-2-amino phenol. 2018;5(8):394–404.
19. Al-Zaidi BH, Hasson MM, Ismail AH. New complexes of chelating Schiffbase: Synthesis, spectral investigation, antimicrobial, and thermal behavior studies. J Appl Pharm Sci. 2019;9(4):45–57.
20. Bayoumi HH, Alaghaz AN, Aljahdali MS. Cu(II), Ni(II), Co(II) and Cr(III) complexes with N_2O_2-chelating schiff's base ligand incorporating azo and sulfonamide moieties: Spectroscopic, electrochemical behavior and thermal decomposition studies. Int J Electrochem Sci. 2013;8(7):9399–413.
21. Soleimani E. Novel Complexes of Mn (II), Co (II), and Cu (II) with Ligand Derived from Dibromobenziloxime. 2010;(Ii):653–8.
22. Nair MS, Arish D, Joseyphus RS. Synthesis, characterization, antifungal, antibacterial and DNA cleavage studies of some heterocyclic Schiff base metal complexes. J Saudi Chem Soc [Internet]. 2012;16(1):83–8. Available from: http://dx.doi.org/10.1016/j.jscs.2010.11.002
23. Wahba OAG, Hassan AM, Naser AM, Hanafi AM. Preparation and Spectroscopic studies of

some copper and nickel schiff base complexes and their applications as colouring pigments in protective paints industry. Egypt J Chem. 2017;60(1):25–40.

24. Lalitha K, Subrahmanyam M, Kumari V. Fe / TiO2 : A Visible Light Active Photocatalyst for the Continuous Production of Hydrogen from Water Splitting Under Solar Irradiation Fe / TiO 2 : A Visible Light Active Photocatalyst for the Continuous Production of Hydrogen from Water Splitting Under . 2014;(February).
25. Modi CK, Trivedi PM. Zeolite-Y entrapped Ru(III) and Fe(III) complexes as heterogeneous catalysts for catalytic oxidation of cyclohexane reaction. Arab J Chem [Internet]. 2017;10:S1452–9. Available from: http://dx.doi.org/10.1016/j.arabjc.2013.03.016
26. Palanimurugan A, Kulandaisamy A. DNA, in vitro antimicrobial/anticancer activities and biocidal based statistical analysis of Schiff base metal complexes derived from salicylalidene-4-imino-2,3-dimethyl-1-phenyl-3-pyrazolin-5-one and 2-aminothiazole. J Organomet Chem [Internet]. 2018;861:263–74. Available from: https://doi.org/10.1016/j.jorganchem.2018.02.051
27. Vairalakshmi m, Princess R, Johnson raja S. the Metal Complexes of Novel Schiff Base Containing Isatin: Characterization, Antimicrobial, Antioxidant and Catalytic Activity Study. Asian J Pharm Clin Res. 2019;12(8):206–10.
28. Sivaprakash G, Tharmaraj P, Jothibasu M, Arun. A. Antimicrobial Analysis of Schiff Base Ligands Pyrazole and Diketone Metal Complex Against Pathogenic Organisms. Int J Adv Res. 2017;5(2):2656–63.
29. Malik MA, Dar OA, Gull P, Wani MY, Hashmi AA. Heterocyclic Schiff Base Transition Metal Complexes in Antimicrobial and Heterocyclic Schiff base transition metal complexes in antimicrobial and anticancer. Medchemcomm [Internet]. 2017;(December). Available from: http://dx.doi.org/10.1039/C7MD00526A
30. Arts CB. Synthesis , Characterization and Antimicrobial Studies of N 1 - [(1 E) -1- (2-Hydroxyphenyl) ethylidene] -2-oxo-2 H -chromene-3-carbohydrazide and its Metal Complexes. 2009;6(3):615–24.
31. Abu-khadra AS, Afify AS, Mohamed A, Farag RS, Hassan Y. Preparation , Characterization and Antimicrobial Activity of Schiff Base of (E) - N - (4- (Thiophen-2-ylmethyleneamino) Phenylsulfonyl) Acetamide Metal Complexes. 2018;1–10.
32. Liu Q, Xie BO, Lin SEN, Liao Q, Deng R, Zhaohua YAN. Silicon-containing diorganotin complexes with salicylaldehyde thiosemicarbazone and their anticancer activity. J Chem Sci [Internet]. 2019;0123456789. Available from: https://doi.org/10.1007/s12039-019-1650-5
33. Xu Y, Meng X. Molecular Simulation Elaborating the Mechanism of 1β-Hydroxy Alantolactone Inhibiting Ubiquitin-Conjugating Enzyme UbcH5s. Sci Rep [Internet].

2020;10(1):1–13. Available from: http://dx.doi.org/10.1038/s41598-019-57104-4

34. Duru Kamaci U, Kamaci M, Peksel A. Thermally Stable Schiff Base and its Metal Complexes: Molecular Docking and Protein Binding Studies. J Fluoresc. 2017;27(3):805–17.

Figures

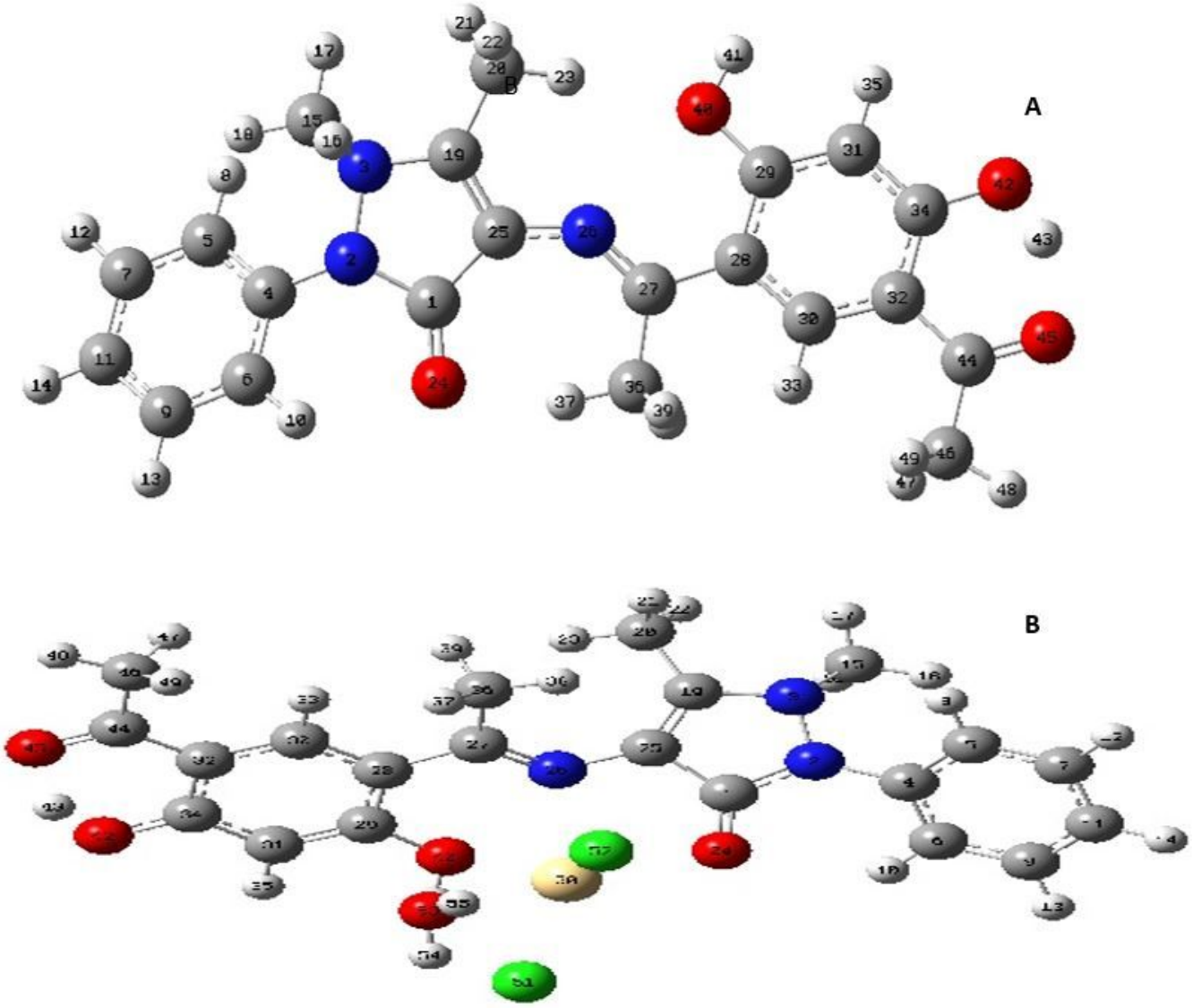

Figure 1

The optimized structures of (A) H2L and (B) Cd(II) complex.

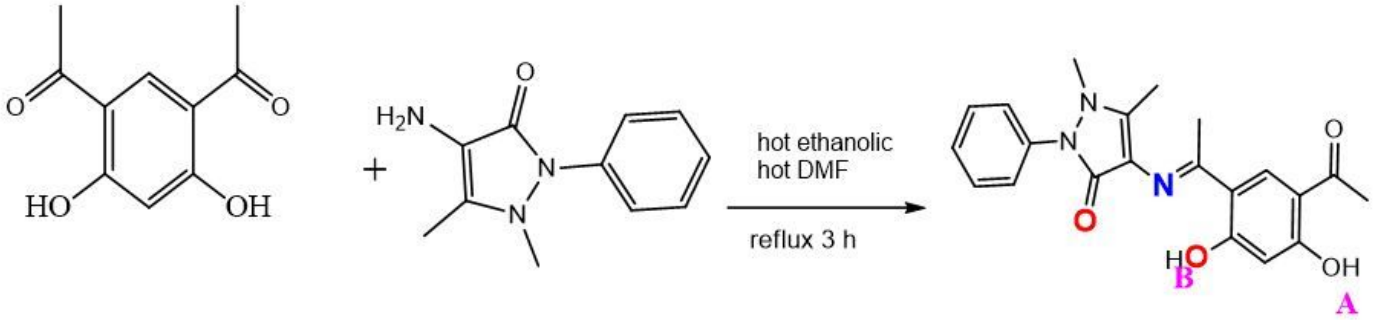

Figure 2

Preparation of the Schiff base ligand.

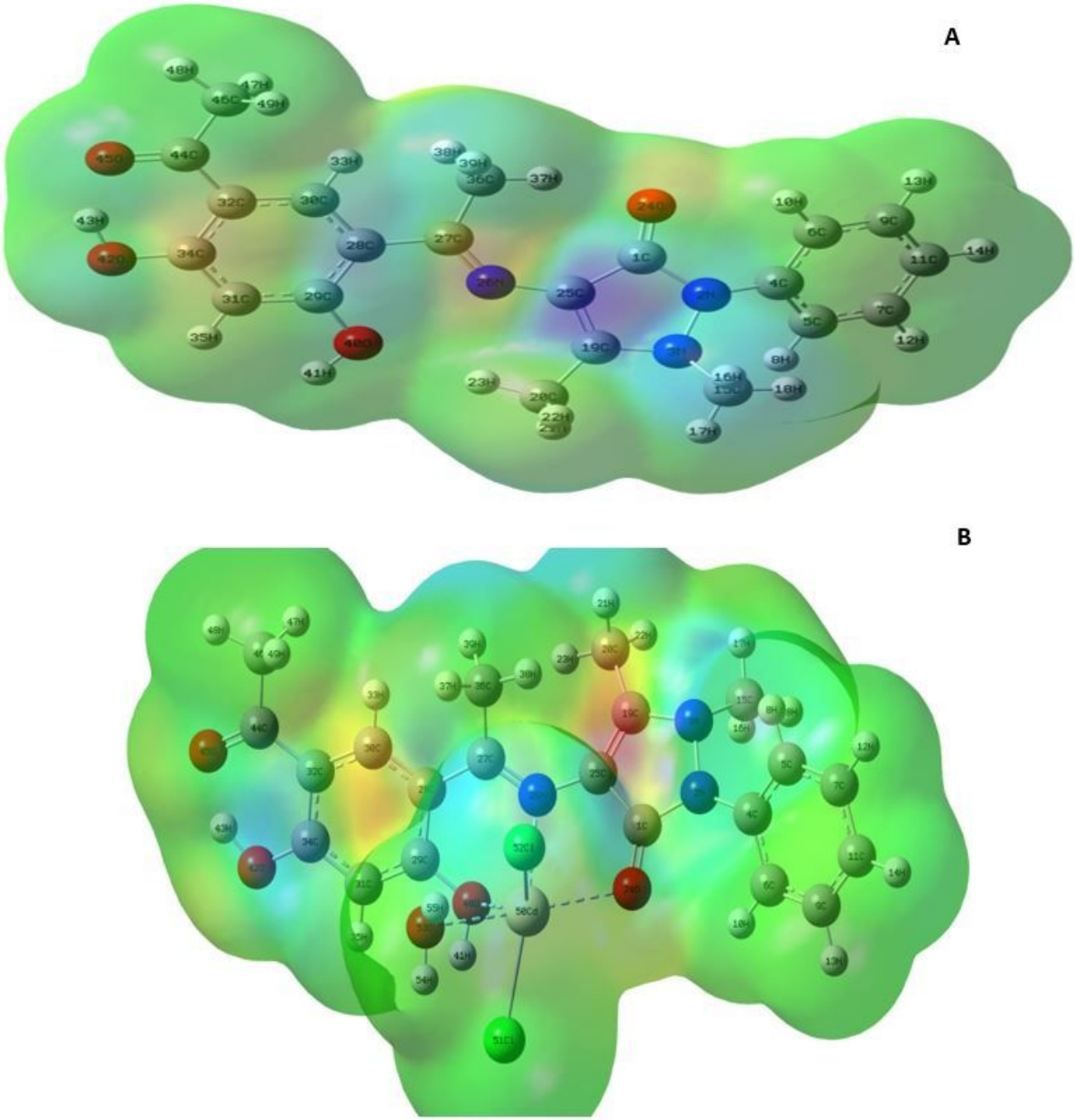

Figure 3

Molecular electrostatic potential map of (A) H2L and (B) [Cd(H2L)(H2O)Cl2] complex. The electron density isosurface is 0.004 a.u.

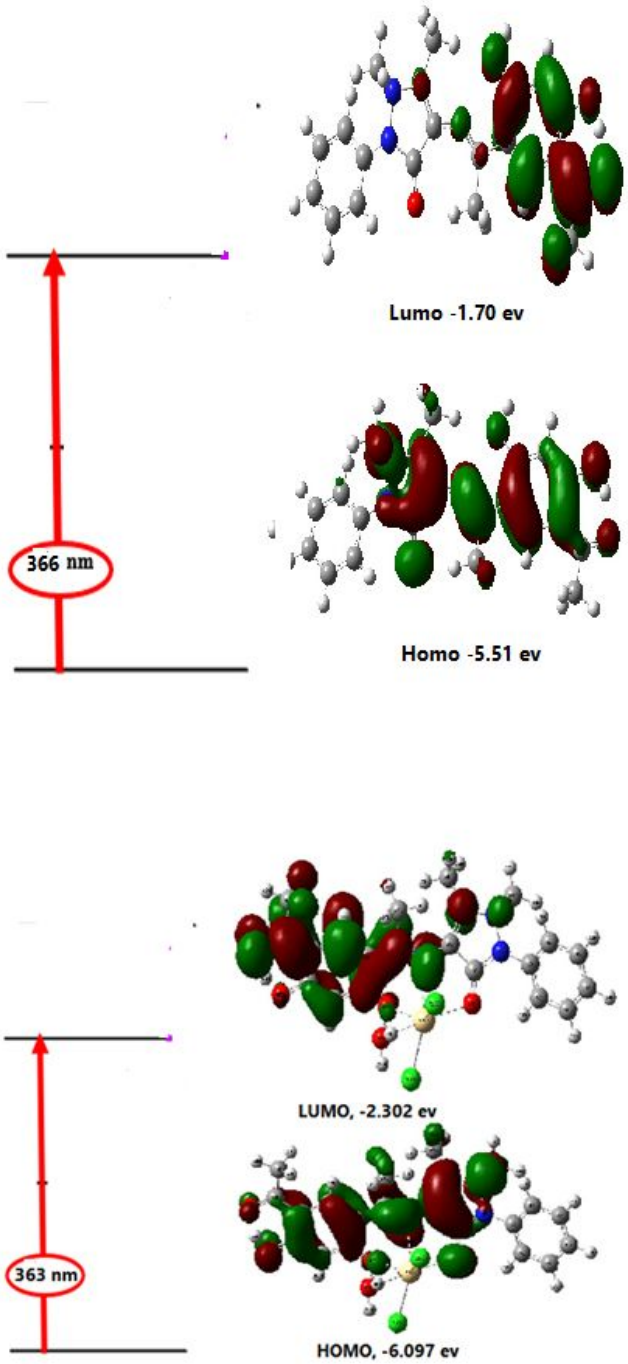

Figure 4

3a. Theoretical electronic absorption transitions for H2L in ethanol solvent. 3b. Theoretical electronic absorption transitions for Cd(II) complex in DMF solvent.

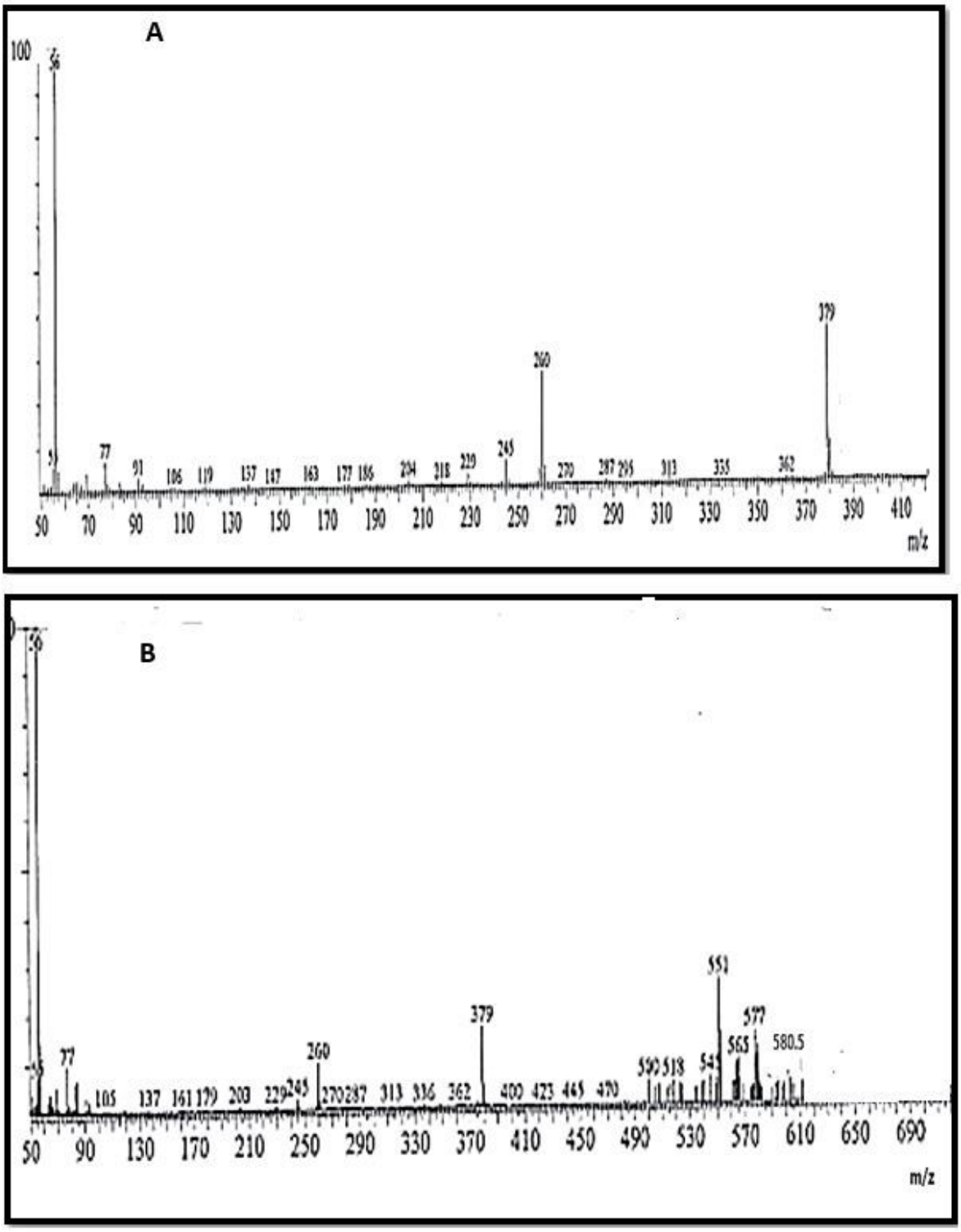

Figure 5

Mass spectra (A) H2L ligand and (B) [Cd(H2L)(H2O)Cl2]complex.

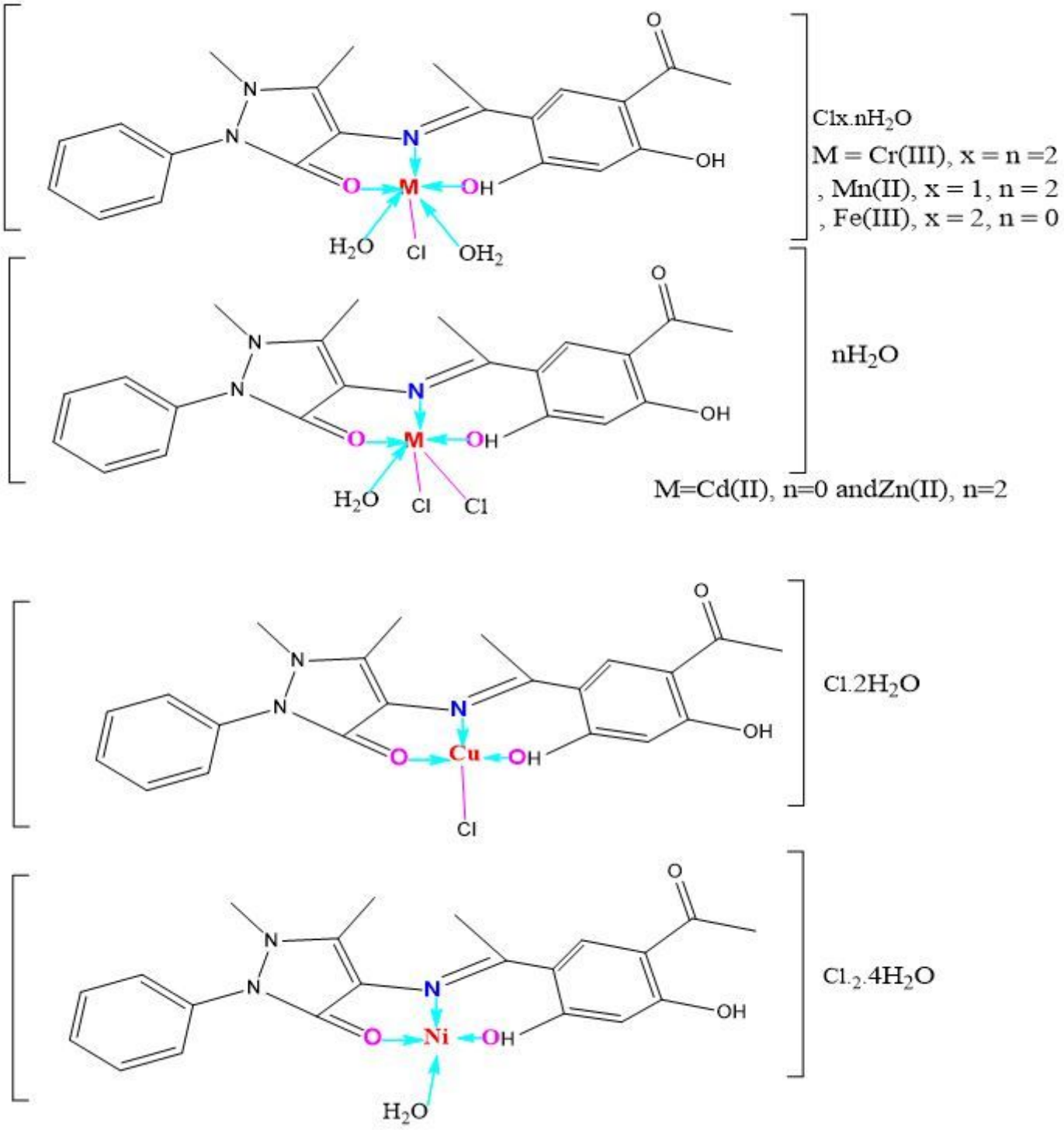

Figure 6

Structures of Schiff base metal complexes.

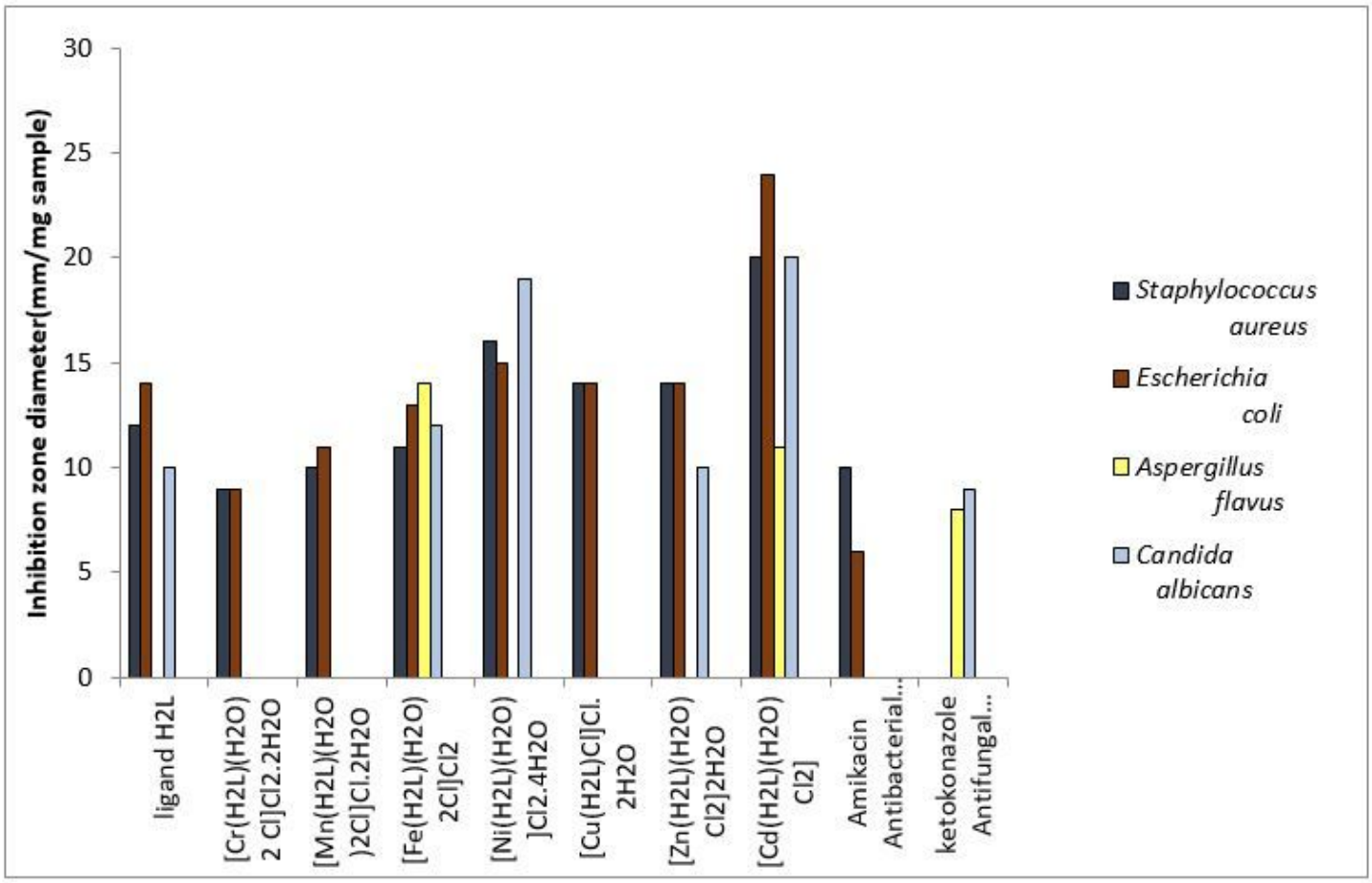

Figure 7

Biological activity of Schiff base ligand (H2L) and its metal complexes.

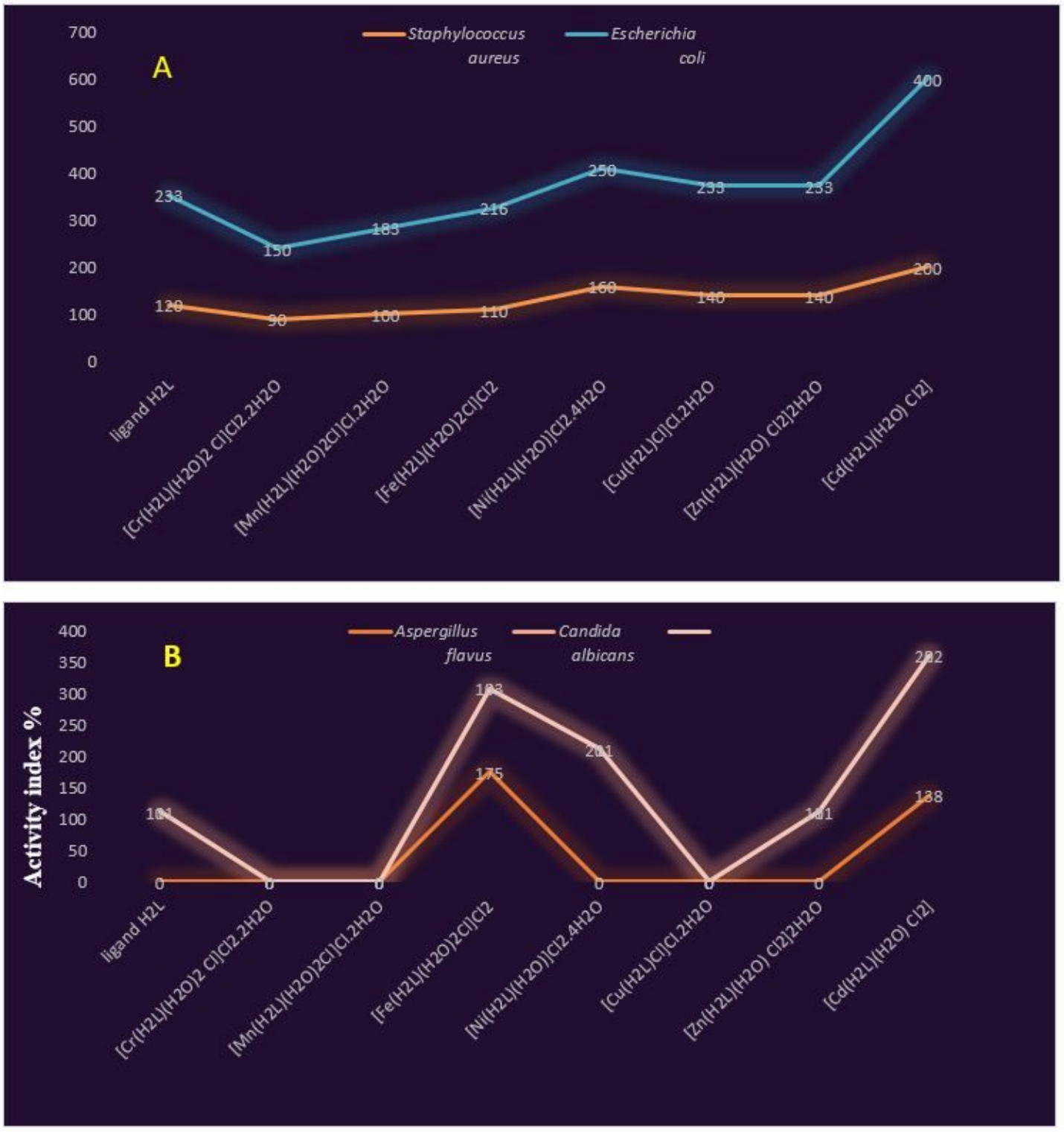

Figure 8

Activity index of Schiff base ligand (H2L) and its metal complexes against (A) different Gram (+ve) and Gram (−ve) bacteria (B) different fungal.

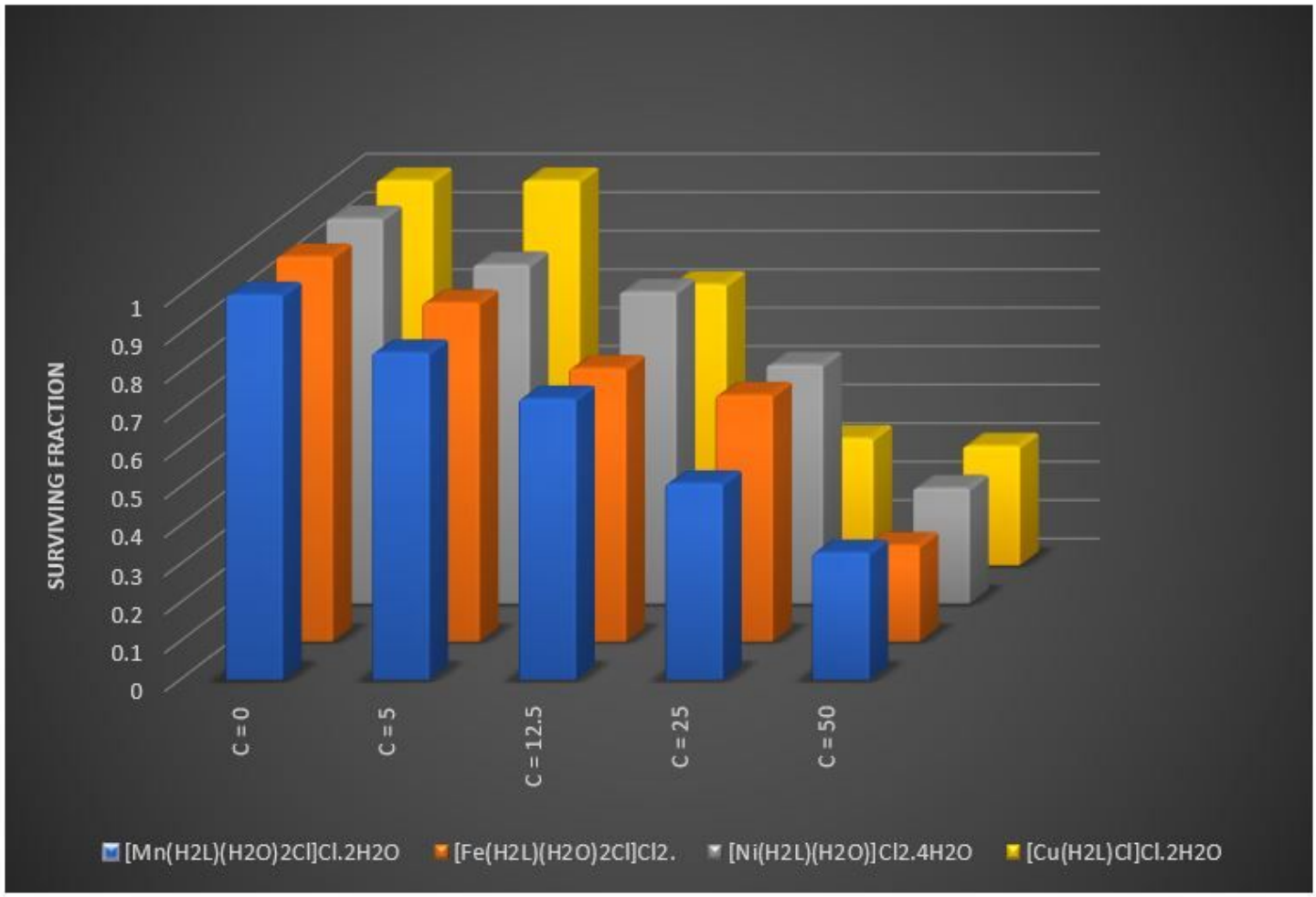

Figure 9

Anticancer effects of Schiff base ligand and its metal complexes in terms of % Cell Inhibition at 100 µg/ml concentration.

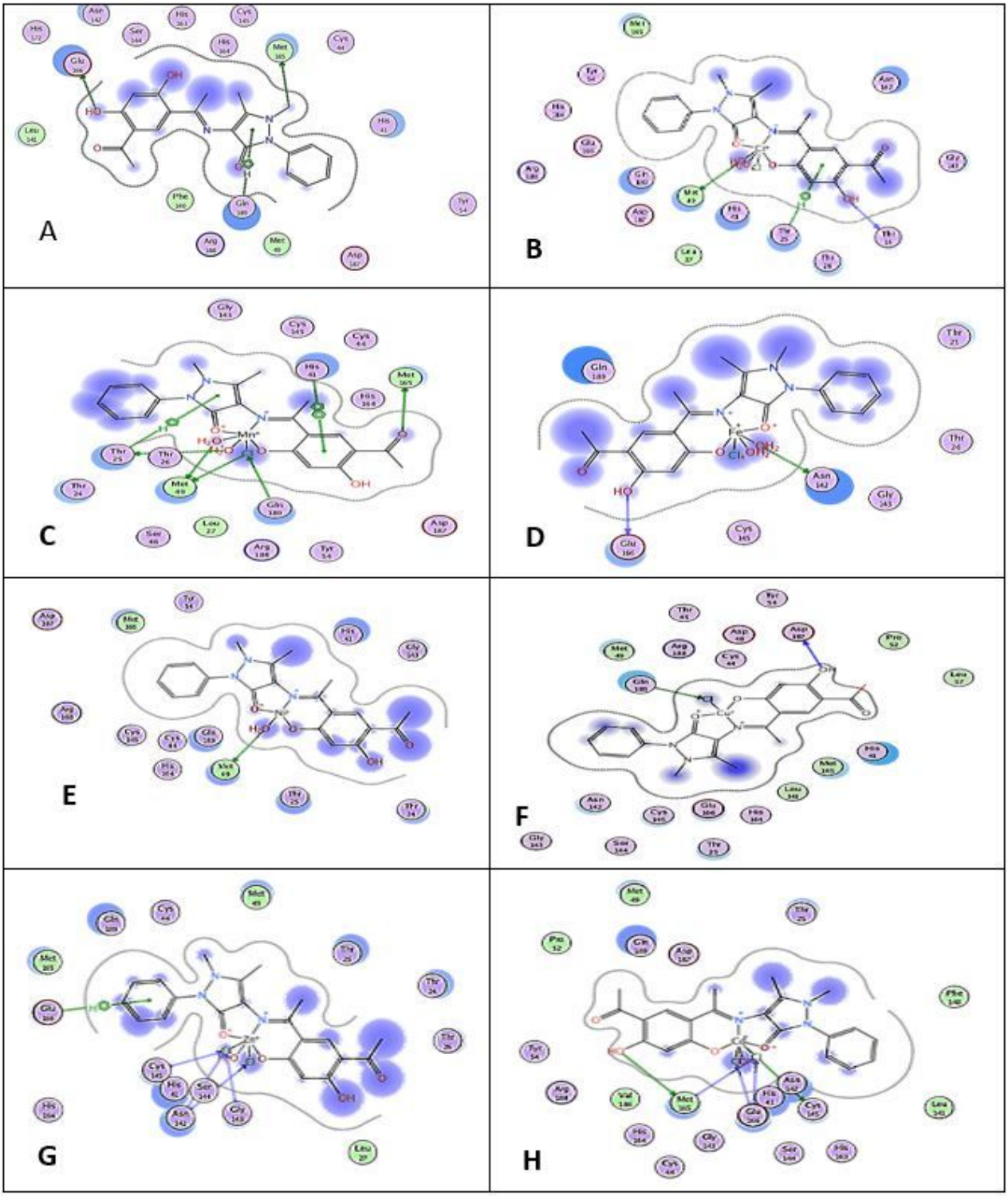

Figure 10

2D Molecular docking simulation studies of hydrophobic interactions of the Schiff base ligand (A)H2L and (B) Cr(III), (C) Mn(II), (D) Fe(III), (E) Ni(II), (F) Cu(II), (G) Zn(II) and (H) Cd(II)with amino acid residues of PDB ID: 6XBH are shown with dotted curves.

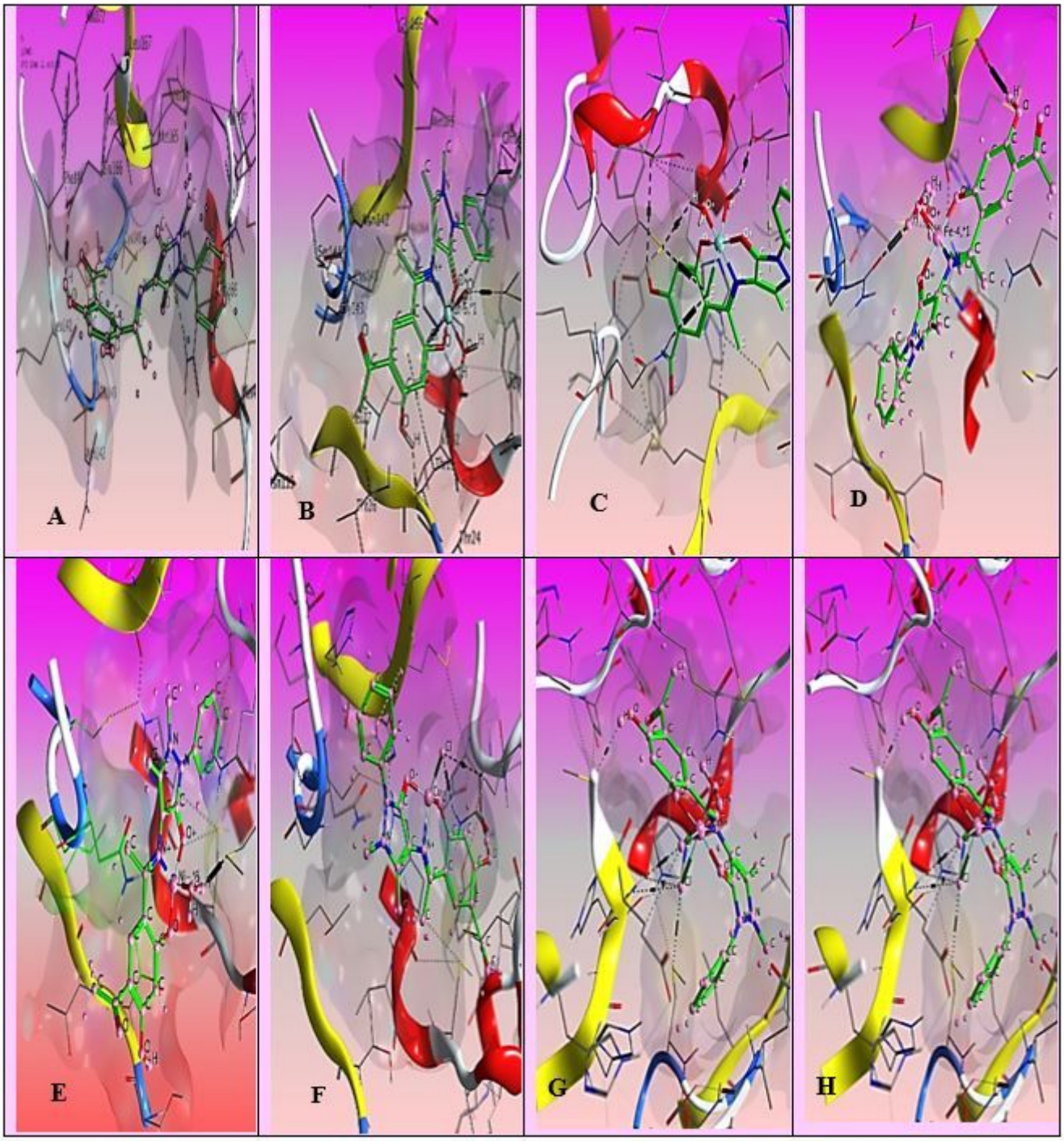

Figure 11

3D Molecular docking simulation studies of the interaction between (A) Schiff base ligand H2L and (B) Cr(III), (C) Mn(II), (D) Fe(III), (E) Ni(II), (F) Cu(II), (G) Zn(II) and (H) Cd(II)with the active site of the receptor of PDB ID: 6XBH. The docked conformation of the compound is shown in ball and stick representation.

Supplementary Files

This is a list of supplementary files associated with this preprint. Click to download.

- Table7.jpg